

Theory and simulation of electroosmotic suppression of acoustic streaming^{a)}

Bjørn G. Winckelmann and Henrik Bruus^{b)}

Department of Physics, Technical University of Denmark, DTU Physics Building 309, DK-2800 Kongens Lyngby, Denmark

ABSTRACT:

Acoustic handling of nanoparticles in resonating acoustofluidic devices is often impeded by the presence of acoustic streaming. For micrometer-sized acoustic chambers, this acoustic streaming is typically driven by viscous shear in the thin acoustic boundary layer near the fluid-solid interface. Alternating current (ac) electroosmosis is another boundary-driven streaming phenomenon routinely used in microfluidic devices for the handling of particle suspensions in electrolytes. Here, we study how streaming can be suppressed by combining ultrasound acoustics and ac electroosmosis. Based on a theoretical analysis of the electrokinetic problem, we are able to compute numerically a form of the electrical potential at the fluid-solid interface, which is suitable for suppressing the typical acoustic streaming pattern associated with a standing acoustic half-wave. In the linear regime, we even derive an analytical expression for the electroosmotic slip velocity at the fluid-solid interface and use this as a guiding principle for developing models in the experimentally more relevant nonlinear regime that occurs at elevated driving voltages. We present simulation results for an acoustofluidic device, showing how implementing a suitable ac electroosmosis results in a suppression of the resulting electroacoustic streaming in the bulk of the device by 2 orders of magnitude.

© 2021 Acoustical Society of America. <https://doi.org/10.1121/10.0005051>

(Received 29 January 2021; revised 27 April 2021; accepted 29 April 2021; published online 4 June 2021)

[Editor: James F. Lynch]

Pages: 3917–3928

I. INTRODUCTION

Acoustofluidics is a rapidly advancing field of research based on the integration of ultrasound and microfluidics in lab-on-a-chip designs. Acoustic waves are used for label-free and efficient particle handling with high biocompatibility, and the principle has found many applications within biotechnology and health care. Examples include acoustic separation,^{1–3} trapping,^{4,5} and tweezing^{6–8} as well as enrichment of cancer cells^{9,10} and bacteria,^{11,12} and size-independent sorting of cells.¹³

System designs for particle migration by ultrasound, termed acoustophoresis, are typically based on long fluid channels with cross section dimensions in the range of 0.1–1 mm. The frequency of the acoustic waves in aqueous suspensions with wavelengths comparable to the chamber dimensions is thus in the low MHz range. These ultrasound fields are generated by piezoelectric transducers. Two competing forces of nonlinear origin act on particles suspended in the fluid. One force is the acoustic radiation force induced by acoustic wave-scattering by the particles.^{14–18} This force focuses particles in nodes or antinodes of the acoustic waves, and it scales with the particle volume.¹⁹ The other force is the viscous Stokes drag due to the acoustic streaming,^{20–23} which scales linearly with the particle radius and tends to swirl particles around. Because of the different scalings, streaming-induced drag force is the

dominating force for particles smaller than a critical size. For an aqueous suspension of spherical polystyrene particles in a 1-MHz ultrasound field, the critical diameter has been determined to be around $2\ \mu\text{m}$.^{24,25} To ease the acoustic manipulation of sub-micromolar particles, such as bacteria, viruses, and exosomes, we seek to suppress the acoustic streaming.

There are two types of acoustic streaming: the boundary-layer-driven streaming originating from the viscous boundary layers near the fluid-solid interfaces, as first analyzed analytically by Lord Rayleigh²⁰ and later studied in more detail,^{23,26–28} and the bulk-driven streaming generated by attenuation of acoustic waves in the bulk of the fluid,²⁹ an effect that is typically negligible in microfluidics except for rotating acoustic fields.³⁰

Electroosmosis, the steady motion of electrolytic solutions with respect to a charged surface by an external electric potential, is another type of boundary-driven streaming.³¹ The principle has been used to create, say, micropumps with no moving parts for lab-on-a-chip systems.^{32–35} In particular, alternating current (ac) electroosmotic pumps have gained attention by generating relevant flow velocities at relatively low ac-voltages without electrolysis, thus circumventing the problem of gas formation. Pumping velocities have been reported in the $\sim 100\ \mu\text{m/s}$ range,^{33,34} which is of similar magnitude to typical acoustic streaming velocities.

In this study, we suggest the combination of acoustic and ac electroosmotic streaming with a resulting net electroacoustic streaming close to zero. As an example of how to achieve this, we propose a specific design of an

^{a)}This paper is part of a special issue on Theory and Applications of Acoustofluidics.

^{b)}Electronic mail: bruus@fysik.dtu.dk, ORCID: 0000-0001-5827-2939.

electroacoustic device consisting of a microchannel with surface electrodes for generating electroosmosis embedded in an elastic solid with an attached piezoelectric transducer for generating acoustics. The analysis is carried out with no intrinsic zeta potential and thus belongs to the body of work that assumes that the chemically generated intrinsic zeta potential has been removed, say by means of a direct current (dc) offset in the applied potential or by chemical surface treatments. A thorough study of the effects of an intrinsic zeta potential is left for future work.

The paper is structured as follows: In Sec. II, we present the general theoretical framework. In Sec. III, we consider ac electroosmosis at low excitation voltages, where the electrokinetic problem can be linearized and analytical expressions for the electroosmotic slip velocity are obtained. In Sec. IV, the analytical solution is compared to full numerical solutions at higher voltages, and we find that the linearized regime captures both qualitative and quantitative behavior at surprisingly high voltages. In Sec. V, the linearized ac electroosmotic theory is integrated into an existing acoustofluidic simulation adapted from Skov *et al.*³⁶ Using an electrode design that could be produced by standard clean room fabrication techniques together with an attached piezoelectric transducer, we demonstrate how to obtain heavily suppressed streaming patterns when exciting both an ac electroosmosis and an ultrasound acoustophoresis. In Sec. VI, we discuss some of the limitations of the proposed model, and finally we conclude.

II. THEORY

The core part of the system we analyze is a binary electrolyte in the form of a dilute aqueous suspension of ions, with a single positive ion (subscript +) and a single negative ion (subscript -) of opposite valences $Z_{\pm} = \pm Z$. The electrolyte is placed inside a microchannel in the presence of a MHz-ultrasound pressure resonance p_1 with angular frequency $\omega_{ac} = 2\pi f_{ac} = 2\pi(1/T_{ac})$ and a kHz-ac electrical potential ϕ with angular frequency $\omega_{eo} = 2\pi f_{eo} = 2\pi(1/T_{eo})$. The fundamental continuum fields in the fluid at point \mathbf{r} and time t are the mass density ρ , the pressure p , the fluid velocity \mathbf{v} , and the viscous stress tensor $\boldsymbol{\sigma}$, as well as the concentration fields of the positive and negative ions c_+ and c_- , the electrical charge density ρ_{el} , and the electric potential $\phi(\mathbf{r}, t)$. The material parameters of the system are the dynamic viscosity η_{fl} , the bulk viscosity η_{fl}^b , the speed of sound c_{fl} , the quiescent mass density ρ_{fl} , the isentropic compressibility κ_{fl} , the ionic valence number Z , the ionic diffusivities D_{\pm} and mobilities μ_{\pm} , and the electric permittivity ϵ_{fl} . The governing equations for the fluid including acoustics are the mass continuity and Navier–Stokes equation,

$$\partial_t \rho = -\nabla \cdot (\rho \mathbf{v}), \quad (1a)$$

$$\partial_t (\rho \mathbf{v}) = -\nabla \cdot [(\rho \mathbf{v}) \mathbf{v}] + \nabla \cdot \boldsymbol{\sigma} - Ze(c_+ - c_-) \nabla \phi, \quad (1b)$$

$$\boldsymbol{\sigma} = -p\mathbf{I} + \eta_{fl} [\nabla \mathbf{v} + (\nabla \mathbf{v})^T] + \frac{3\eta_{fl}^b - 2\eta_{fl}}{3} \nabla \cdot \mathbf{v} \mathbf{I}. \quad (1c)$$

The electrokinetics of the ions are governed by the concentration continuity, Nernst, and Poisson equation,

$$\partial_t c_{\pm} = -\nabla \cdot \mathbf{J}_{\pm}, \quad (2a)$$

$$\mathbf{J}_{\pm} = c_{\pm} \mathbf{v} - D_{\pm} \nabla c_{\pm} - \mu_{\pm} c_{\pm} \nabla \phi, \quad (2b)$$

$$\nabla^2 \phi = -\frac{1}{\epsilon_{fl}} Ze(c_+ - c_-). \quad (2c)$$

The fields $Q(\mathbf{r}, t)$ will be treated in perturbation theory written as

$$Q(\mathbf{r}, t) = Q_0(\mathbf{r}) + \text{Re}[Q_1(\mathbf{r}) e^{-i\omega t}] + Q_2(\mathbf{r}, t). \quad (3)$$

Here, Q_0 is the unperturbed field, Q_1 is the first-order acoustic and electric time-harmonic perturbation, and Q_2 is the unsteady second-order field, which is generated by the inherent nonlinearities in hydrodynamic and electrokinetic equations. The time-averaged second-order response is defined as $\langle Q_2(\mathbf{r}, t) \rangle = (\omega/2\pi) \int_0^{2\pi/\omega} Q_2(\mathbf{r}, t) dt$. A time-average of a product of two first-order fields is also a second-order term, written as $\langle \text{Re}[A_1 e^{-i\omega t}] \text{Re}[B_1 e^{-i\omega t}] \rangle = \frac{1}{2} \text{Re}[A_1 B_1^*]$, where the asterisk denotes complex conjugation.

A. Combined acoustics and ac electroosmosis

We consider a microfluidic system with integrated acoustics and electroosmosis as sketched conceptually in Fig. 1. A piezoelectric transducer actuates the system acoustically and generates acoustic streaming, and electrode arrays surrounding the fluid channel actuate ac electroosmotic streaming, which by proper design aims to counteract and suppress the acoustic streaming. To provide a proof of concept of this streaming suppression, we consider a simple long, straight rectangular fluid channel of dimensions $W \times H = 375 \times 160 \mu\text{m}^2$. The acoustic problem in this configuration has previously been studied extensively both theoretically and experimentally,^{19,24,37,38} and it is known that the physical properties of the system are well-described by modeling restricted to the two-dimensional (2D) cross section. We thus apply a Cartesian (y, z) coordinate system

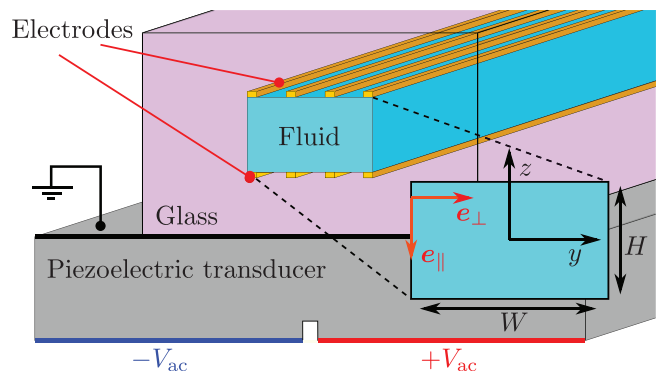


FIG. 1. (Color online) A sketch of the proposed electroacoustic device: a microchannel in glass with integrated acoustics and electroosmosis. Electrode arrays with ac-voltage V_{eo} are implemented at the fluid-solid interface to induce the ac electroosmosis, and a piezoelectric transducer with ac-voltage V_{ac} is glued to the bottom of the device to generate acoustics.

centered in the fluid channel. The equilibrium position of the fluid-solid interface will be denoted s_0 , and to describe boundary effects, we apply a local coordinate system ($\mathbf{e}_\parallel, \mathbf{e}_\perp$) at the boundary.

Combining the two phenomena could potentially lead to non-trivial coupled effects. When acoustic waves travel through an ionic suspension, the ions will oscillate slightly out of phase with respect to the solvent. The different mobilities of ionic species will lead to a so-called ionic vibration potential. These potentials normalized by the oscillatory velocity of the fluid are typically on the order of $1 \text{ mV}/(1 \text{ m/s})$.³⁹ This effect is around 2 orders of magnitude lower than what is needed for acoustic streaming suppression by electroosmosis, and it is thus ignored.

As we shall see in the following, ac electroosmotic flows work ideally for $f_{\text{eo}} \sim 1 \text{ kHz}$, whereas the acoustic actuation frequencies are 1000 times faster in the range of $f_{\text{ac}} \sim 1 \text{ MHz}$. This separation of time scales allows us to use the acoustomechanical responses at the time-averaged (with respect to T_{ac}) spatial position of the fluid-solid interface and the oscillating fluid, when computing the electrokinetic responses. Furthermore, the electrokinetic flow is established through the ionic Debye layer at the fluid-solid boundary on the short length scale $\lambda_D \sim 10 \text{ nm}$, whereas the acoustically induced velocity fields are established over a viscous boundary layer of the much longer length scale $\delta \sim 500 \text{ nm}$. Thus, we assume that no significant advection of ions in the Debye layer happens due to the acoustic streaming or vibrational velocity. This spatiotemporal decoupling of the electrokinetics and acoustics is further supported by the fact that both electroosmotic and acoustic streaming in microchannels are described by linear Stokes flows,^{28,32} so we conclude that the combined electroacoustic streaming can be derived simply by superimposing the two flows computed separately.

Last, as the electric field extends throughout the fluid, dielectrophoretic forces inevitably arise and act on suspended particles.⁴⁰ For most materials in the present context, these forces are several orders of magnitude lower than the acoustic radiation force and the drag forces from streaming. We therefore ignore dielectrophoresis in this analysis.

B. Pressure acoustics with viscous boundary layers

To simulate acoustic fields, we follow the approach of Refs. 28 and 36. The simulations of the linearized models presented below in Secs. II, III, and V were validated by performing mesh convergence tests as described in Ref. 24 to ensure numerical convergence below 1%. For more details, see the supplementary material.⁴¹

The complex amplitude of the mechanical displacement field in the surrounding solid of the fluid channel and in the piezoelectric transducer is denoted \mathbf{u}_1 . The complex acoustic pressure field and the associated oscillating fluid velocity field are denoted p_1 and \mathbf{v}_1 , respectively. The steady time-averaged acoustic streaming $\langle \mathbf{v}_2^{\text{ac}} \rangle$ and the corresponding

pressure $\langle p_2^{\text{ac}} \rangle$ are then calculated as a Stokes flow with an acoustic slip velocity $\langle \mathbf{v}_{2,\text{slip}}^{\text{ac}} \rangle$ at the boundary,

$$0 = \nabla \cdot \langle \mathbf{v}_2^{\text{ac}} \rangle, \tag{4a}$$

$$\mathbf{0} = -\nabla \langle p_2^{\text{ac}} \rangle + \eta_\Pi \nabla^2 \langle \mathbf{v}_2^{\text{ac}} \rangle + \frac{\Gamma_\Pi \omega_{\text{ac}}}{2c_\Pi^2} \text{Re}[p_1^* \mathbf{v}_1], \tag{4b}$$

$$\langle \mathbf{v}_2^{\text{ac}} \rangle = \langle \mathbf{v}_{2,\text{slip}}^{\text{ac}} \rangle, \text{ for } \mathbf{r} = \mathbf{s}_0. \tag{4c}$$

In Eq. (4b), the acoustic body force, with the small viscous bulk damping coefficient $\Gamma_\Pi = [\frac{4}{3}\eta_\Pi + \eta_\Pi^b]\kappa_\Pi\omega_{\text{ac}} \ll 1$, is typically negligible for single mode operation in microchannels,³⁰ and the flow is thus mostly driven by the slip velocity $\langle \mathbf{v}_{2,\text{slip}}^{\text{ac}} \rangle$. Throughout this work, we consider the conventional standing half-wave mode in the acoustic pressure. As we demonstrate later, the acoustic slip velocity for this mode closely resembles that of the classical Rayleigh streaming in fluid channels etched into acoustically hard materials like Pyrex glass,

$$\langle \mathbf{v}_{2,\text{slip}}^{\text{ac}} \rangle_{z=\pm \frac{1}{2}H} \approx \mathbf{e}_y v_2^{\text{Rayl}} \sin(2k_0 y), \tag{5a}$$

$$v_2^{\text{Rayl}} = \frac{3E_{\text{ac}}}{2\rho_\Pi c_\Pi}, \tag{5b}$$

where E_{ac} is the average acoustic energy density,

$$E_{\text{ac}} = \int_{-W/2}^{W/2} \int_{-H/2}^{H/2} \left[\frac{1}{4} \rho_\Pi |\mathbf{v}_1|^2 + \frac{1}{4} \kappa_\Pi |p_1|^2 \right] \frac{dy dz}{HW}. \tag{6}$$

To determine the suppression of streaming numerically, we seek to minimize the spatial average, the norm $\|\mathbf{v}\|$, of the steady streaming \mathbf{v}_2 in the fluid cross section,

$$\|\mathbf{v}\| = \int_{-W/2}^{W/2} \int_{-H/2}^{H/2} |\langle \mathbf{v}(y, z) \rangle| \frac{dy dz}{HW}. \tag{7}$$

Inspired by Bach and Bruus,⁴² the streaming suppression is also quantified by the measure,

$$S_q = \int_{-W/2}^{W/2} \int_{-H/2}^{H/2} \Theta \left(\frac{q}{100} v_2^{\text{Rayl}} - |\langle \mathbf{v} \rangle| \right) \frac{dy dz}{HW}, \tag{8a}$$

$$\Theta(x) = \begin{cases} 0, & x < 0, \\ 1, & x \geq 0. \end{cases} \tag{8b}$$

For the initial part of our study, we employ the analytically known acoustic resonance mode derived by Bach and Bruus,²⁸ where the side walls are oscillated as

$$\mathbf{u}_1 \left(\pm \frac{1}{2}W, z \right) = d_0 \cos \left(\sqrt{-\frac{(1+i)\delta}{H}} \frac{\omega_{\text{ac}}}{c_\Pi} z \right) e^{-i\omega_{\text{ac}} t} \mathbf{e}_y. \tag{9}$$

Here, d_0 is the displacement amplitude, which is tuned to reach a desired average energy density or acoustic streaming. Given the physical parameters used for our study and

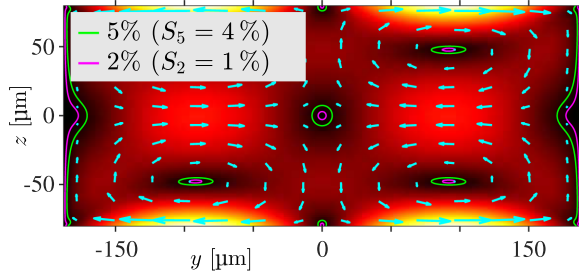


FIG. 2. (Color online) Numerical simulation without including electrokinetics of the normalized streaming $\langle v_2^{\text{ac}} \rangle / v_2^{\text{Rayl}}$ [see Eq. (5b), cyan vectors] generated by the acoustic standing half-wave in the hard-wall rectangular cross section $W \times H = 375 \times 160 \mu\text{m}^2$ using the side-wall actuation (9). The color plot is the magnitude $|\langle v_2^{\text{ac}} \rangle| / v_2^{\text{Rayl}}$ from 0 (black) to 1 (white). The 5% (green) and 2% (magenta) contour lines are shown with the corresponding suppression values S_5 and S_2 ; see Eq. (8a).

listed in the supplementary material,⁴¹ the resonance frequency for water at 25 °C is $f_{\text{ac}}^{\text{res}} = 1.993 \text{ MHz}$. The well-known acoustic streaming pattern generated by this actuation is shown in Fig. 2.

C. ac electroosmosis

We consider an aqueous solution of a simple binary salt, say KCl, with ionic charges $Z_{\pm} = \pm Z$, concentrations c_{\pm} , diffusivities D_{\pm} , and electric mobilities μ_{\pm} . We also introduce the average diffusivity $D = \frac{1}{2}(D_+ + D_-)$, which turns out to be the lowest-order correction to asymmetric ions in the linearized theory given below. All parameter values are listed in the supplementary material.⁴¹

We largely follow the presentations given in Refs. 32 and 43 but consider a more general externally applied electric potential at the fluid-solid interface,

$$V_{\text{ext}}(s_0, t) = \text{Re}[V_{\text{eo}} w(s_0) e^{-i\omega_{\text{eo}} t}]. \quad (10)$$

Here, $w(s_0)$ is some complex-valued function of order unity that describes the shape of the externally applied potential at the boundary, whereas V_{eo} describes its amplitude. We consider flow velocities v^{eo} of sufficiently low amplitudes to describe the fluid as incompressible and drop the nonlinear term in the momentum equation, Eq. (1b). The electric potential is denoted ϕ_{fl} in the fluid and ϕ_{sl} in the surrounding solid and piezoceramic. The full set of governing equations for the electrokinetic problem in the fluid are thus written as

$$\partial_t c_{\pm} = -\nabla \cdot \mathbf{J}_{\pm}, \quad \text{with } \nabla \cdot v^{\text{eo}} = 0, \quad (11a)$$

$$\mathbf{J}_{\pm} = c_{\pm} v^{\text{eo}} - D_{\pm} \nabla c_{\pm} - \mu_{\pm} c_{\pm} \nabla \phi_{\text{fl}}, \quad (11b)$$

$$\nabla^2 \phi_{\text{fl}} = -\frac{1}{\epsilon_{\text{fl}}} Z e (c_+ - c_-), \quad (11c)$$

$$\rho_{\text{fl}} \partial_t v^{\text{eo}} = -\nabla p^{\text{eo}} + \eta_{\text{fl}} \nabla^2 v^{\text{eo}} - Z e (c_+ - c_-) \nabla \phi_{\text{fl}}. \quad (11d)$$

The boundary condition for the electrokinetic problem on electrode surfaces $\partial\Omega_{\text{eo}}$ is an equipotential condition and

on dielectric surfaces $\partial\Omega_{\text{di}}$ a zero-charge condition. All fluid-solid interfaces admit zero ionic flux normal to the wall (we adopt the notation $\partial_{\perp} = \mathbf{e}_{\perp} \cdot \nabla$ and $\partial_{\parallel} = \mathbf{e}_{\parallel} \cdot \nabla$), and the fluid velocity field must fulfill the no slip boundary condition,

$$\phi_{\text{fl}}(s_0, t) = V_{\text{ext}}(s_0, t), \quad s_0 \in \partial\Omega_{\text{eo}}, \quad (12a)$$

$$\epsilon_{\text{fl}} \partial_{\perp} \phi_{\text{fl}} = \epsilon_{\text{sl}} \partial_{\perp} \phi_{\text{sl}}, \quad s_0 \in \partial\Omega_{\text{di}}, \quad (12b)$$

$$v^{\text{eo}}(s_0, t) = \mathbf{0}, \quad (12c)$$

$$\mathbf{e}_{\perp} \cdot \mathbf{J}_{\pm}(s_0, t) = 0. \quad (12d)$$

III. LINEARIZED ANALYSIS OF AC ELECTROOSMOSIS

The nonlinear nature of Eq. (11) makes it computationally and analytically challenging to work with general electrokinetic problems. For most computations, we opt to use a linearized theory, which heavily reduces the computational footprint. In Sec. IV, we address the error introduced by using this theory at higher voltages. A conceptual sketch of electroosmotic flow generation is shown in Fig. 3. The general idea is to generate an electric charge density at electrode surfaces and then induce a boundary-driven flow by dragging the ions along the surface with a parallel electric field.

A. Linearized electrokinetic equations

We consider the special case where $D_{\pm} = D$ such that the Einstein relation implies $\mu_+ = -\mu_- = \mu$,

$$\mu_{\pm} = \pm \frac{Z D_{\pm}}{V_T}, \quad \text{with } V_T = \frac{k_B T}{e}, \quad (13)$$

where k_B is the Boltzmann constant, T is the temperature, and $V_T \approx 26 \text{ mV}$ is the thermal voltage. Following the treatment in Ref. 43, we consider a zero intrinsic zeta potential and the linearized dynamical Debye–Hückel regime, which is obtained for weak externally applied potentials $V_{\text{eo}} \ll V_T$ at the electrode surfaces. Here, the applied potential and the corresponding changes in ionic densities act as first-order fields. Through the nonlinear electric body force, this will generate steady streaming as well as double-harmonic streaming with frequency $2\omega_{\text{eo}}$, similar to perturbative

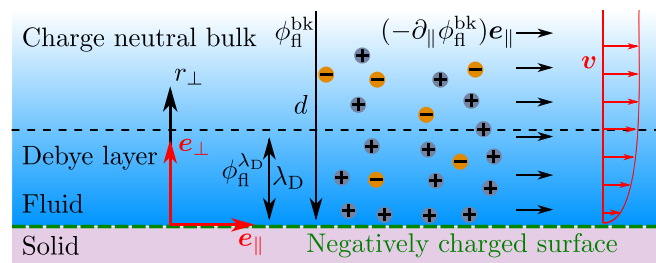


FIG. 3. (Color online) Conceptual drawing of electroosmosis at a flat boundary. Ions are pulled toward a charged surface, resulting in a thin layer of excess charge density termed the Debye layer. An electric field parallel to the surface is in turn established to pull on the charge density, which drives a flow through the electric body force present in the Debye layer.

acoustic calculations. Denoting the initial ionic concentration by c_0 , we write

$$c_{\pm} = c_0 + \text{Re}[c_{1\pm} e^{-i\omega_{\text{eo}}t}], \quad |c_{1\pm}| \ll c_0, \quad (14a)$$

$$\phi_{\text{fl}} = \text{Re}[\phi_{1,\text{fl}} e^{-i\omega_{\text{eo}}t}], \quad \mathbf{v}^{\text{eo}} = \mathbf{v}_2^{\text{eo}}(\mathbf{r}, t), \quad p^{\text{eo}} = p_2^{\text{eo}}(\mathbf{r}, t). \quad (14b)$$

The second-order electric field and ionic concentrations are omitted, as they do not affect the electroosmotic streaming. We then apply the linearization $c_{\pm} \nabla \phi_{\text{fl}} \approx c_0 \nabla \phi_{1,\text{fl}}$ and $c_{\pm} \mathbf{v}^{\text{eo}} \approx 0$ in Eq. (11b), where the latter is valid in the diffusive limit, where ionic advection becomes insignificant compared to diffusion. The first-order electrodynamic fields and the steady time-averaged second-order flow are thus obtained from⁴³

$$-i\omega_{\text{eo}} \nu_1 = D \nabla^2 \nu_1 - \omega_D \nu_1, \quad (15a)$$

$$\nabla^2 \phi_{1,\text{fl}} = -\frac{1}{\epsilon_{\text{fl}}} Z e \nu_1, \quad (15b)$$

$$0 = \nabla \cdot \langle \mathbf{v}_2^{\text{eo}} \rangle, \quad (15c)$$

$$\mathbf{0} = -\nabla \langle p_2^{\text{eo}} \rangle + \eta_{\text{fl}} \nabla^2 \langle \mathbf{v}_2^{\text{eo}} \rangle - \frac{Z e}{2} \text{Re}[\nu_1 \nabla \phi_{1,\text{fl}}^*], \quad (15d)$$

where we have introduced the notation

$$\nu_1 = c_{1+} - c_{1-}, \quad \omega_D = \frac{D}{\lambda_D^2}, \quad \lambda_D = \sqrt{\frac{\epsilon_{\text{fl}} k_B T}{2(Ze)^2 c_0}}. \quad (16)$$

Correspondingly, the boundary condition (12d) becomes

$$\mathbf{e}_{\perp} \cdot \left[\nabla \nu_1 + \frac{\epsilon_{\text{fl}}}{Ze \lambda_D^2} \nabla \phi_{1,\text{fl}} \right] = 0, \quad \text{for } \mathbf{r} = \mathbf{s}_0. \quad (17)$$

B. Effective ac electrokinetic theory

The rectangular cross section $W \times H$ of Fig. 2 only contains planar fluid-solid interfaces, and the potential-shape function $w(s_0)$ of Eq. (10) is assumed to vary on length scales comparable to the chamber dimensions $\partial_{\parallel} w(s_0) \sim \frac{1}{d} w(s_0)$, where $d \sim W, H$. Further, we assume that $\omega_{\text{eo}} \ll \omega_D$, which is the relevant limit for our purpose. When an external potential is applied at the fluid-solid interface, ions will accumulate at the wall in a thin layer of length scale λ_D . This ionic layer will completely screen off the wall potential for dc wall potentials, but for ac potentials the screening is only partial. Because $\lambda_D \ll d$, we have $\nabla^2 \sim \partial_{\perp}^2$ in Eq. (15a). The perpendicular coordinate away from the surface is called r_{\perp} , and thus

$$\nu_1(\mathbf{r}) = \nu_0 w(s_0) e^{-\kappa r_{\perp}}, \quad \text{with } \kappa = \frac{1}{\lambda_D} \sqrt{1 - i \frac{\omega_{\text{eo}}}{\omega_D}}, \quad (18)$$

where ν_0 is a constant. The solution for $\phi_{1,\text{fl}}$ will contain a particular solution $\phi_{1,\text{fl}}^{\lambda_D}$, which reflects the partial ionic screening in the thin Debye layer near the boundary, and a homogeneous solution $\phi_{1,\text{fl}}^{\text{bk}}$ that extends into the bulk,

$$\phi_{1,\text{fl}}(\mathbf{r}) = \phi_{1,\text{fl}}^{\lambda_D}(\mathbf{r}) + \phi_{1,\text{fl}}^{\text{bk}}(\mathbf{r}). \quad (19)$$

Combining Eqs. (15b) and (18) and inserting $\nabla^2 \phi_{1,\text{fl}}^{\lambda_D} \sim \partial_{\perp}^2 \phi_{1,\text{fl}}^{\lambda_D}$, the two terms in Eq. (19) obey

$$\phi_{1,\text{fl}}^{\lambda_D}(\mathbf{r}) = -\nu_0 \frac{Ze}{\epsilon_{\text{fl}} \kappa^2} w(s_0) e^{-\kappa r_{\perp}}, \quad (20a)$$

$$\nabla^2 \phi_{1,\text{fl}}^{\text{bk}} = 0. \quad (20b)$$

Using boundary conditions (12a) and (17) with Eqs. (18), (19), and (20a) inserted at Ω_{eo} , we eliminate ν_0 to find

$$\phi_{1,\text{fl}}^{\text{bk}}(s_0) = V_{\text{eo}} w(s_0) + \frac{i}{\kappa} \frac{\omega_D}{\omega_{\text{eo}}} \partial_{\perp} \phi_{1,\text{fl}}^{\text{bk}}(s_0), \quad s_0 \in \Omega_{\text{eo}}, \quad (21a)$$

$$\nu_1(\mathbf{r}) = i \frac{\omega_D}{\omega_{\text{eo}}} \frac{\epsilon_{\text{fl}} \kappa}{Ze} \partial_{\perp} \phi_{1,\text{fl}}^{\text{bk}}(s_0) e^{-\kappa r_{\perp}}, \quad (21b)$$

$$\phi_{1,\text{fl}}^{\lambda_D}(\mathbf{r}) = -i \frac{\omega_D}{\omega_{\text{eo}}} \frac{1}{\kappa} \partial_{\perp} \phi_{1,\text{fl}}^{\text{bk}}(s_0) e^{-\kappa r_{\perp}}. \quad (21c)$$

For dielectric surfaces Ω_{di} , the boundary condition (12b) can similarly be rewritten in terms of $\phi_{1,\text{fl}}^{\text{bk}}$,

$$\epsilon_{\text{sl}} \partial_{\perp} \phi_{\text{sl}}(s_0) = \left(1 + i \frac{\omega_D}{\omega_{\text{eo}}} \right) \epsilon_{\text{fl}} \partial_{\perp} \phi_{1,\text{fl}}^{\text{bk}}(s_0), \quad s_0 \in \Omega_{\text{di}}. \quad (22)$$

The known forms of ν_1 and $\phi_{1,\text{fl}}^{\lambda_D}$ can be inserted in Eq. (15d) alongside the calculated $\phi_{1,\text{fl}}^{\text{bk}}$. With this, to lowest order in λ_D/d and $\omega_{\text{eo}}/\omega_D$, the steady time-averaged streaming $\langle \mathbf{v}_2^{\text{eo}} \rangle$ is a simple Stokes flow with an electroosmotic slip velocity $\langle \mathbf{v}_{2,\text{slip}}^{\text{eo}} \rangle$ given by $\phi_{1,\text{fl}}^{\text{bk}}$,

$$0 = \nabla \cdot \langle \mathbf{v}_2^{\text{eo}} \rangle, \quad (23a)$$

$$\mathbf{0} = \eta_{\text{fl}} \nabla^2 \langle \mathbf{v}_2^{\text{eo}} \rangle - \nabla \langle p_2^{\text{eo}} \rangle, \quad (23b)$$

$$\langle \mathbf{v}_2^{\text{eo}} \rangle_{s_0} = \langle \mathbf{v}_{2,\text{slip}}^{\text{eo}} \rangle, \quad (23c)$$

$$\langle \mathbf{v}_{2,\text{slip}}^{\text{eo}} \rangle = -\mathbf{e}_{\parallel} \frac{\epsilon_{\text{fl}} \omega_D}{2 \eta_{\text{fl}} \omega_{\text{eo}}} \text{Re} \left[\frac{i}{\kappa} \partial_{\perp} \phi_{1,\text{fl}}^{\text{bk}} (\partial_{\parallel} \phi_{1,\text{fl}}^{\text{bk}})^* \right]_{s_0}. \quad (23d)$$

This form of the slip velocity is essentially identical to the one given in Eq. (2) of Ref. 32.

C. The analytic electrokinetic double mode

To generate an ac electroosmotic slip velocity $\langle \mathbf{v}_{2,\text{slip}}^{\text{eo}} \rangle$ opposite to the acoustic Rayleigh slip velocity (5), we use an analytical model in the linearized regime as guidance. We consider an idealized case, where a perfectly smooth

potential is generated at the fluid boundary, corresponding to the limit of implementing infinitely many infinitely thin electrodes in our electrode arrays. The more realistic case of a finite amount of electrodes is subsequently assessed in Sec. V.

In an experimental setup (see Fig. 1), it would likely be desirable to only implement electrodes at the top and bottom boundaries ($y, \pm \frac{1}{2}H$) of the microchannel and thus assume a zero-charge condition at the side walls ($\pm \frac{1}{2}W, z$). The electric potential in the surrounding solid originates from the same electrodes that generate the fluid potential, which leads to $\phi_{sl} \sim \phi_{1,fl}^{bk}$. Because most relevant materials for creating microfluidic channels have $\epsilon_{sl} \ll \epsilon_{fl}$, Eq. (22) dictates $\partial_{\perp} \phi_{1,fl}^{bk} \approx 0$ at a dielectric boundary.

A single sinusoidal mode in the electric potential is studied in Ref. 43 and is shown to give a negligible steady streaming component. Since $\kappa \approx 1/\lambda_D$ for $\omega_{eo} \ll \omega_D$, it is clear from Eq. (23d) that a phase difference is needed between the perpendicular and the parallel component of the electric bulk field $\mathbf{E}^{bk} = -\nabla \phi_{1,fl}^{bk}$ at the boundary s_0 to generate a significant steady streaming $\langle \mathbf{v}_2^{eo} \rangle$. This is not possible with a single mode, so instead we combine two sinusoidal modes with a relative phase difference ϑ ,

$$\partial_{\perp} \phi_{1,fl}^{bk,n} \left(\pm \frac{1}{2}W, z \right) = 0, \quad (24a)$$

$$w \left(y, \pm \frac{1}{2}H \right) = \sin(k_n y) + e^{i\vartheta} \sin(k_{n+1} y), \quad (24b)$$

$$\text{with } k_n = \frac{2n+1}{W} \pi, \quad \text{for } n = 0, 1, 2, \dots \quad (24c)$$

We use $\kappa \approx 1/\lambda_D$ and derive the analytical solution of Eqs. (20b) and (21a) for the bulk potential $\phi_{1,fl}^{bk,n}(y, z)$,

$$\begin{aligned} \phi_{1,fl}^{bk,n}(y, z) = & \frac{V_{eo} \cosh(k_n z) \sin(k_n y)}{\cosh\left(k_n \frac{H}{2}\right) + i \frac{\omega_n}{\omega_{eo}} \sinh\left(k_n \frac{H}{2}\right)} \\ & + \frac{e^{i\vartheta} V_{eo} \cosh(k_{n+1} z) \sin(k_{n+1} y)}{\cosh\left(k_{n+1} \frac{H}{2}\right) + i \frac{\omega_{n+1}}{\omega_{eo}} \sinh\left(k_{n+1} \frac{H}{2}\right)}, \end{aligned} \quad (25a)$$

$$\text{with } \omega_n = k_n \lambda_D \omega_D, \quad \text{for } n = 0, 1, 2, \dots \quad (25b)$$

Inserting this $\phi_{1,fl}^{bk,n}$ in Eq. (23d) leads to an expression for the electroosmotic slip velocity $\langle \mathbf{v}_{2,slip}^{eo} \rangle$, with an amplitude that depends on both ϑ and ω_{eo} . We are interested in generating large streaming amplitudes at low applied voltages. The phase difference that leads to the largest streaming amplitude is denoted $\vartheta = \vartheta_n^{opt}$, and the optimized angular frequency at ϑ_n^{opt} is denoted $\omega_{eo} = \omega_{n,eo}^{opt}$. These can both be found analytically and result in the electroosmotic slip velocity,

$$\langle \mathbf{v}_{2,slip}^{eo} \rangle \Big|_{y=\pm W/2} = \mathbf{0}, \quad (26a)$$

$$\langle \mathbf{v}_{2,slip}^{eo} \rangle \Big|_{z=\pm H/2} = -g_n(y) v_n^{eo} \mathbf{e}_y, \quad (26b)$$

$$g_n(y) = \frac{\sinh(k_0 H) \sin(k_{2n+(3/2)} y) + \sinh\left(k_{n+(1/2)} \frac{H}{2}\right) \sin(2k_0 y)}{\frac{1}{2n+2} \sinh(k_0 H) + \sinh\left(k_{n+(1/2)} \frac{H}{2}\right)},$$

$$v_n^{eo} = \frac{\pi \epsilon_{fl} V_{eo}^2 (2n+1)(2n+3)}{8 \eta_{fl} W (n+1)}. \quad (26c)$$

The optimal phase difference ϑ_n^{opt} and the corresponding optimal angular frequency $\omega_{n,eo}^{opt}$ are given by

$$\vartheta_n^{opt} = \pi - \arctan(\alpha_n), \quad (27a)$$

$$\alpha_n = \frac{1 + \frac{\omega_n \omega_{n+1}}{\omega_{eo}^2} \tanh\left(k_n \frac{H}{2}\right) \tanh\left(k_{n+1} \frac{H}{2}\right)}{\frac{\omega_{n+1}}{\omega_{eo}} \tanh\left(k_{n+1} \frac{H}{2}\right) - \frac{\omega_n}{\omega_{eo}} \tanh\left(k_n \frac{H}{2}\right)}, \quad (27b)$$

$$\omega_{n,eo}^{opt} = \sqrt{\omega_n \omega_{n+1} \tanh\left(\frac{1}{2} k_n H\right) \tanh\left(\frac{1}{2} k_{n+1} H\right)}. \quad (27c)$$

The slip velocity $\langle \mathbf{v}_{2,slip}^{eo} \rangle$ in Eq. (26) approaches the desired acoustic slip velocity $-\langle \mathbf{v}_{2,slip}^{ac} \rangle$ of Eq. (5a) for large values of n . Even for $n=1$, the $\sin(2\pi y/W)$ term will dominate for $H \sim W$. The streaming amplitude is seen to increase linearly with n for large values of n . This continuous growth is caused by the increase in the transverse electrical bulk field generated by the sinusoidal modes for a given surface potential amplitude. By superimposing the acoustics simulation of Fig. 4(a) with the electrokinetic simulation of Fig. 4(b) using the boundary conditions (24) and $n=1$, where for our channel dimensions $\omega_{1,eo}^{opt} = 6731 \text{ s}^{-1}$ and $\vartheta_1^{opt} = 1.883$, we obtain the resulting suppressed electroacoustic streaming shown in Fig. 4(c). For $E_{ac} = 100 \text{ J/m}^3$, the streaming is optimally suppressed through the electroosmotic mode discussed above at $V_{eo} = 127 \text{ mV}$. We see that the streaming is suppressed below 5% of the Rayleigh

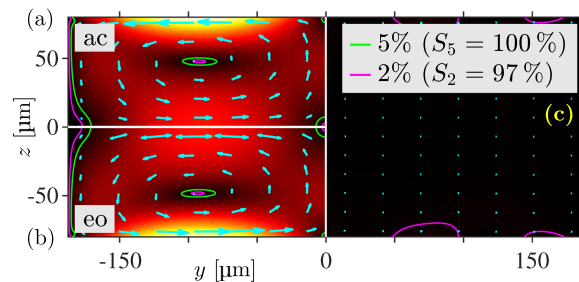


FIG. 4. (Color online) Numerical simulation of the electroacoustic streaming $\langle \mathbf{v}_2 \rangle$ plotted as in Fig. 2 using the linearized model of Sec. III C in a channel with hard walls: (a) The purely acoustic streaming $\langle \mathbf{v}_2^{ac} \rangle$ defined in Fig. 2 with $E_{ac} = 100 \text{ J/m}^3$. (b) The purely electroosmotic streaming $\langle \mathbf{v}_2^{eo} \rangle$ generated by the boundary conditions (24) driven at $V_{eo} = 127 \text{ mV}$. (c) The electroacoustic streaming $\langle \mathbf{v}_2 \rangle = \langle \mathbf{v}_2^{eo} \rangle + \langle \mathbf{v}_2^{ac} \rangle$ is suppressed by tuning $V_{eo} = 127 \text{ mV}$ to match $E_{ac} = 100 \text{ J/m}^3$.

streaming amplitude everywhere in the channel, and almost the entire streaming pattern is suppressed below 2%. This result constitutes our first proof of concept of suppression of acoustic streaming by electroosmotic streaming.

Let us discuss the assumptions. It takes very high values of n to violate the assumption $\lambda_D \ll d$, and using high order sinusoidal modes could be a valid strategy for creating powerful streaming. However, doing this with discrete electrode arrays would require many electrodes, and in practice it may be desirable to use low order modes. For $n = 1$, we find $|\langle v_{2,\text{slip}}^{\text{eo}} \rangle|_{\text{max}} \approx 6 \text{ nm/s}$ for $V_{\text{eo}} = 1 \text{ mV}$. Extrapolating to higher voltages, one would need around $V_{\text{eo}} = 130 \text{ mV}$ to reach typical acoustic streaming velocities of around $100 \text{ } \mu\text{m/s}$. This obviously violates the assumption of $V_{\text{eo}} \ll V_T$ but still remains well below the steric regime.⁴⁴

The efficiency of the electric double-mode potential stems from a phase-matching between the charge density generated by one mode and the electric field of the other mode, which drags the established charge density along the top and bottom surfaces of the channel.

Last, we note that the suggested mode combination is not the only way of generating the desired streaming pattern. A combination between a sinusoidal and a linear mode with dielectric side walls also generates a useful streaming pattern, albeit the analytical solution becomes more complicated. If one controls the potential on the side walls, it also becomes possible to generate clean sinusoidal modes with an even number of half-waves. However, these possibilities are not explored in this study.

IV. NONLINEAR ELECTROOSMOTIC FLOWS

To reach experimentally relevant streaming velocities, one needs to apply voltages around $V_{\text{eo}} \sim 5V_T$, well into the nonlinear regime of the electrokinetic problem. In the following, we evaluate the capability of the linearized theory of ac electrokinetics to predict qualitative trends for higher voltages. We adopt a numerical approach inspired by Muller *et al.*³⁸ to compare the linear predictions to the full nonlinear system of Eq. (11). For lower voltages, where the linearized theory is valid, we assume the streaming velocity v^{eo} and corresponding pressure p^{eo} to be of the form³⁸

$$\mathbf{a}(\mathbf{r}, t) = \mathbf{a}_2^0(\mathbf{r}, t) + \mathbf{a}_2^{2\omega_{\text{eo}}}(\mathbf{r}, t) \cos(2\omega_{\text{eo}}t), \quad (28)$$

where the time dependencies in \mathbf{a}_2^0 and $\mathbf{a}_2^{2\omega_{\text{eo}}}$ describe a transient period. For higher voltages, a more general time dependency could arise by significant mixing of Fourier components through the nonlinear terms in Eqs. (11b) and (11d). Using a fifth-order Romberg integration scheme,^{38,45} the time-averaged response at a given time t is computed numerically as

$$\langle \mathbf{a}(\mathbf{r}, t) \rangle = \int_{t-(1/2)T_{\text{eo}}}^{t+(1/2)T_{\text{eo}}} \mathbf{a}(\mathbf{r}, t') dt'. \quad (29)$$

A. Numerical implementation

The governing equations (11) are solved with the commercial finite element software COMSOL Multiphysics.⁴⁶ Solving the full time-dependent nonlinear equations increases the computational footprint significantly compared to the linearized treatment. We simulate the transient leading to the time-harmonic problem discussed in the linearized scheme above. The boundary condition (24b) with $n = 1$ is used directly as formulated in Eqs. (10) and (12a). The boundary condition (24a) for the side walls is replaced by

$$\partial_{\perp} \phi_n \left(\pm \frac{1}{2} W, z, t \right) = 0. \quad (30)$$

The two symmetry lines $y = 0$ and $z = 0$ were used to reduce the computational domain by a factor of 4. This is illustrated in Fig. 5(a) alongside the corresponding symmetry boundary conditions. A structured mesh with 60 layers of width $\frac{1}{4} \lambda_D$ was placed parallel to the domain boundaries to fully resolve the thin Debye layer, which now has to be taken into account numerically.

As in Ref. 38, a time-dependent solver is employed with the generalized alpha time-stepping scheme, where the alpha factor is set to 0.5. A constant time stepping of $\Delta t = \frac{1}{256} T_{\text{eo}}$ was used for all simulations. For simulations with $V_{\text{eo}} > 1 \text{ mV}$, the system Jacobian was set to update at every time step to stabilize the solutions. The amplitude of the external voltage $\tilde{V}_{\text{eo}}(t)$ was gradually ramped up through the first oscillation period as

$$\tilde{V}_{\text{eo}}(t) = \frac{1}{2} [1 + \tanh(5\omega_{\text{eo}}t - 3)] V_{\text{eo}}. \quad (31)$$

The time-dependent solver was run for four electric periods, $0 < t < 4T_{\text{eo}}$, and as the physical system is not resonant, a steady state was reached already for $t \simeq 2T_{\text{eo}}$. Here, we present two different simulations, one linear with $V_{\text{eo}} = 0.04V_T = 1 \text{ mV}$ and the other nonlinear with $V_{\text{eo}} = 4.8V_T = 125 \text{ mV}$. The time-averaged solution of the latter, which took eight days to compute, turned out to contain higher-than-second-order harmonics with a relative amplitude of about 1%, signalling the onset of the strongly nonlinear regime. However, due to their relatively low amplitude, these are not discussed further.

The mesh element size in the bulk was $4.2 \text{ } \mu\text{m}$ for $V_{\text{eo}} = 1 \text{ mV}$ and $1.6 \text{ } \mu\text{m}$ for $V_{\text{eo}} = 125 \text{ mV}$, resulting in meshes with 9547 and 28 833 elements, respectively. To validate the nonlinear model at $V_{\text{eo}} = 125 \text{ mV}$, the bulk element size was reduced to $0.8 \text{ } \mu\text{m}$, and the model was run until $t = 0.5 T_{\text{eo}}$. The streaming amplitudes calculated with these two meshes were compared for each time step in a grid of 375×161 points, showing an average relative difference lower than 0.5×10^{-6} between the two meshes at all individual time steps.⁴¹

B. Results of time-dependent simulations

The simulation at $V_{\text{eo}} = 1 \text{ mV}$ was primarily made to check the numerical setup. In Fig. 5(b), the time-averaged

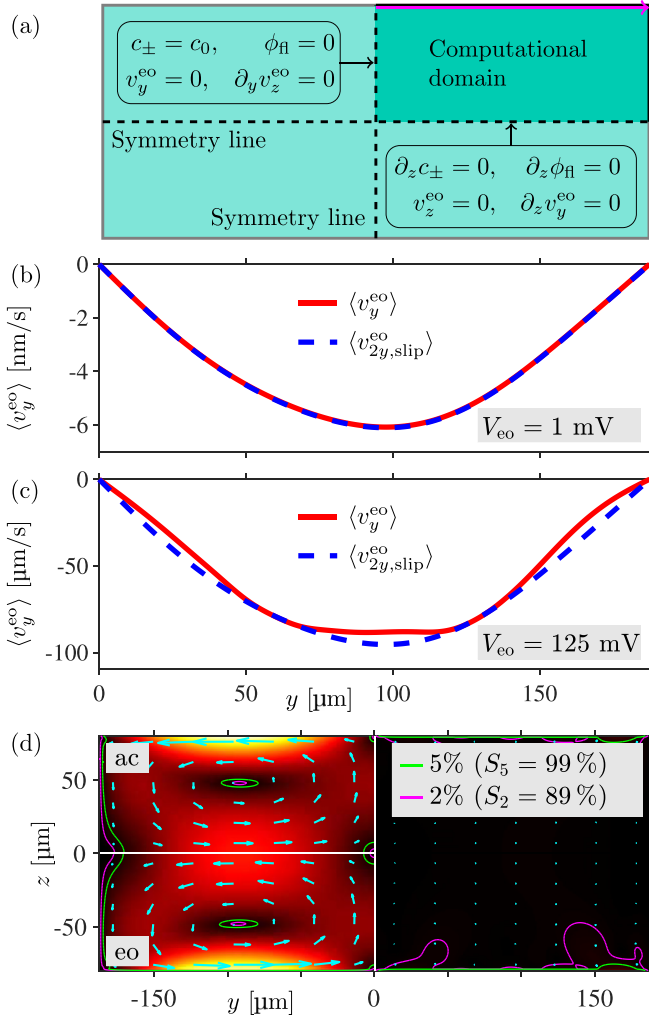


FIG. 5. (Color online) (a) The computational domain defined by the symmetry lines with corresponding boundary conditions. The magenta line at $z = \frac{1}{2}H - 7\lambda_D$ is used in (b) and (c). (b) The time-averaged y-component $\langle v_y^{eo} \rangle$ for $3T_{eo} < t < 4T_{eo}$ of the time-dependent electroosmotic velocity $v^{eo}(t)$ plotted along the magenta line defined in (a) and compared to the analytical slip velocity $\langle v_{2y,slip}^{eo} \rangle$ (26) (dashed blue line) from the linearized model. Both are driven at $V_{eo} = 1$ mV using the boundary conditions obtained by combining Eqs. (24b), (10), and (12a) with $n = 1$. (c) As in (b), but for the much higher driving voltage $V_{eo} = 125$ mV. (d) as in Fig. 4, but now using the nonlinear model to compute $\langle v^{eo} \rangle$ at $V_{eo} = 125$ mV and then tuning the acoustic energy density to $E_{ac} = 91 \text{ J/m}^3$ to optimize the suppression of the electroacoustic streaming $\langle v_2 \rangle = \langle v^{eo} \rangle + \langle v_2^{ac} \rangle$.

horizontal velocity component $\langle v_y^{eo} \rangle$ at $t = 3.5 T_{eo}$ is shown along the top right boundary, marked by the magenta arrow in Fig. 5(a). Specifically, the field is shown just outside the Debye layer at coordinates $(y, z) = (y, \frac{1}{2}H - 7\lambda_D)$, and the comparison with the analytical expression (26b) for the linearized slip velocity $\langle v_{2,slip}^{eo} \rangle$ shows an almost perfect agreement.

A similar plot is made for $V_{eo} = 125$ mV in Fig. 5(c), and there a notable difference between the two theories appears. The peak amplitude of the time-dependent simulation is $88 \mu\text{m/s}$, whereas the linearized theory predicts $95 \mu\text{m/s}$, 8% higher. We notice, however, that clear quantitative and even decent qualitative features remain.

Finally, in Fig. 5(d) the time-averaged nonlinear electroosmotic flow $\langle v^{eo} \rangle$ at $V_{eo} = 125$ mV is superposed with the idealized acoustic streaming $\langle v_2^{ac} \rangle$ at $E_{ac} = 91 \text{ J/m}^3$, in a case chosen to minimize the resulting electroacoustic streaming $\langle v \rangle = \langle v^{eo} \rangle + \langle v_2^{ac} \rangle$. As for the linear case [Fig. 4(c)], the nonlinear streaming in Fig. 5(d) is seen to be heavily suppressed. However, in contrast to the linearized streaming, small patches of streaming extend from the boundary, where the time-dependent solution is seen to differ the most from the linearized theory. Nevertheless, the streaming is less than 2% of the Rayleigh value v_2^{Rayl} in 89% of the domain.

This brief study of electroosmotic streaming in the moderately nonlinear regime suggests that the linearized theory captures the main features of the streaming to a satisfactory degree at the suggested voltage range from 0 to 125 mV for the initial study presented in this work. We therefore return to the computationally much simpler linearized model in Sec. V, where we extend our model to include the elastic channel walls, a small number of surface electrodes, and the piezoelectric transducer.

V. NUMERICAL 2D DEVICE SIMULATIONS

As sketched in Fig. 1, a typical acoustophoretic device contains a microchannel embedded in an elastic solid that is glued onto a piezoelectric transducer. Consequently, the acoustic response including the streaming is degraded compared to the ideal hard-wall system studied above. Moreover, it is not possible in a real electroosmotic device to create and control a given continuous shape of the surface potential, and instead only a limited number of finite-sized electrodes may be fabricated. In the following, we study, through 2D numerical simulations using the linearized electrokinetic model, to what extent the introduction of these more realistic aspects of the model will diminish the ability to suppress the acoustic streaming by electroosmotic streaming.

A. The design of the 2D device

We consider the 2D model sketched in Fig. 6. It contains a microchannel of dimensions $W \times H = 375 \times 160 \mu\text{m}^2$ filled with a dilute aqueous solution of KCl ions and embedded in an elastic block of Pyrex glass of dimensions $H_{Py} \times W_{Py} = 3 \times 1.5 \text{ mm}^2$. The electroosmotic streaming is actuated by voltages on the arrays of N_{elec} rectangular electrodes of dimensions $W_{elec} \times H_{elec}$ ($H_{elec} = 2 \mu\text{m}$ and W_{elec} varied) and spacings of dimension W_{space} embedded in the top and bottom fluid-solid interfaces. The acoustic streaming is actuated by the attached piezoelectric transducer of dimensions $W_{Pz26} \times H_{Pz26} = 5 \times 1 \text{ mm}^2$ modeled as the piezoelectric material Pz26 driven by the potential $\pm V_{ac}$. A central cut of dimensions $W_{cut} \times H_{cut} = 160 \times 375 \mu\text{m}^2$ is made in the bottom of the transducer to enable antisymmetric actuation.⁴⁷

To avoid excessive meshing in the numerical model near the electrodes at the fluid-solid interface, their thickness was chosen to be $2 \mu\text{m}$, which is about 40 times larger

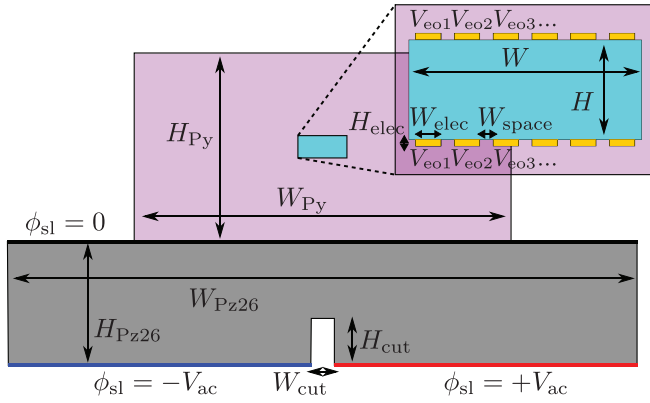


FIG. 6. (Color online) Sketch of the 2D cross section of the simulated electroacoustic device consisting of a microchannel embedded in an elastic solid with surface electrodes and driven acoustically by an attached piezoelectric transducer with a split bottom-electrode for antisymmetric actuation. The relevant length scales and electrode potentials are labeled.

than standard clean-room-deposited electrodes typically having a thickness of 50 nm. Since these enhanced electrodes still comprise a small fraction of the glass volume, they have a negligible effect on the resulting acoustic resonance properties of the channel. Acoustically, the electrodes are part of the elastic solid, and electrically, they are modeled as ideal conductors having equipotential surfaces with the applied voltages $V_{eo1}, V_{eo2}, \dots, V_{eo, N_{elec}}$, respectively, where V_1 is applied to the outermost left electrodes at the top and bottom surfaces. The electrode and spacing widths are always chosen such that $N_{elec}(W_{elec} + W_{space}) = W$ with $W_{space} = \frac{1}{2}W_{elec}$. The y-coordinates of the electrode centers y_m for $m = 1, 2, \dots, N_{elec}$ and the potential $V_{eo,m}$ applied to the electrode arrays, a discretized version of the potential shape (24b) for $n = 1$, are then given by

$$y_m = \frac{2m - 1 - N_{elec}}{2N_{elec}}W, \quad m = 1, 2, \dots, N_{elec}, \quad (32a)$$

$$V_{eo,m} = V_{eo} \left[\sin(k_1 y_m) + e^{i\theta_1^{opt}} \sin(k_2 y_m) \right]. \quad (32b)$$

The optimized parameters θ_1^{opt} and $\omega_{1, eo}^{opt}$ are used in all simulations. The side walls and electrode spacings will have a Pyrex/water interface with the boundary condition described by Eq. (22).

The system is actuated acoustically by potentials applied to the top and bottom boundaries of the piezoelectric transducer at a numerically determined resonance frequency $f_{ac}^{res} = 2.06$ MHz. A voltage difference of $2V_{ac}$ is applied between the two bottom electrodes on the transducer, while the top electrode is grounded. V_{ac} is chosen to reach an average acoustic energy density of $E_{ac} = 100$ J/m³.

B. Simulation results for the 2D device

In the following, we simulate the combined acoustic and electroosmotic streaming as the Stokes flow (4) with its acoustic body force and acoustic slip, but now also adding

the electrokinetics (20b) including the electroosmotic slip velocity (23d),

$$0 = \nabla \cdot \langle \mathbf{v}_2 \rangle, \quad (33a)$$

$$\mathbf{0} = -\nabla \langle p_2 \rangle + \eta_{fl} \nabla^2 \langle \mathbf{v}_2 \rangle + \frac{\Gamma_{fl} \omega_{ac}}{2c_{fl}^2} \text{Re}[p_1^* \mathbf{v}_1], \quad (33b)$$

$$0 = \nabla^2 \phi_{1, fl}^{bk}, \quad (33c)$$

$$\phi_{1, fl}^{bk} = V_{eo} w(s_0) + \frac{i}{K} \frac{\omega_D}{\omega_{eo}} \partial_{\perp} \phi_{1, fl}^{bk}, \quad s_0 \in \Omega_{eo} \quad (33d)$$

$$\langle \mathbf{v}_2 \rangle = \langle \mathbf{v}_{2, slip}^{ac} \rangle + \langle \mathbf{v}_{2, slip}^{eo} \rangle, \quad \text{for } \mathbf{r} = s_0. \quad (33e)$$

One could worry about using the electroosmotic slip velocity for discrete electrodes, where the edges of these equipotential surfaces introduce length scales that violate the assumptions necessary to derive Eqs. (21a) and (23d). A 2D Debye layer forms at the electrode edges, when the linearized system of equations (15) is solved with boundary conditions Eqs. (12a) and (17) and a fully resolved boundary layer. This error only occurs at a relatively small part of the computational domain as long as $W_{elec} \gg \lambda_D$. It was checked numerically that the implementation of the effective boundary conditions only leads to a relative error of 0.8% in the streaming pattern for a simple simulation with only two electrodes of widths $W_{elec} = 10$ μ m.

The 2D device simulation was performed for an increasing number of electrodes ranging from $N_{elec} = 6$ with $W_{elec} = 41.7$ μ m to $N_{elec} = 25$ with $W_{elec} = 10.0$ μ m. For each value of N_{elec} , the voltage was changed to minimize streaming at $E_{ac} = 100$ J/m³. This in turn required a decreasing amplitude for the applied voltage from $V_{eo} = 222$ mV at $N_{elec} = 6$ to $V_{eo} = 162$ mV at $N_{elec} = 25$. Unsurprisingly, it requires a higher voltage to generate streaming through the discrete electrode pattern compared to the idealized mode.

In Fig. 7, we plot the quantitative measures of the obtained streaming suppression versus the number N_{elec} of electrodes in the arrays. Notably, the initial increase from 6 to 10 electrodes yields the largest increase in the suppression measures, after which a gradual saturation sets in. This

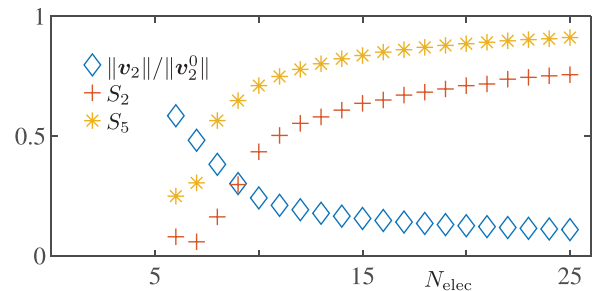


FIG. 7. (Color online) Plots of the streaming suppression for the 2D model defined in Fig. 6 versus the number N_{elec} of electrodes in terms of the quantities S_2 and S_5 of Eq. (8), as well as the normalized streaming value $\|\mathbf{v}_2\|/\|\mathbf{v}_2^0\|$, where $\|\mathbf{v}_2^0\|$ is the norm (7) of the purely acoustic streaming found for $N_{elec} = 0$.

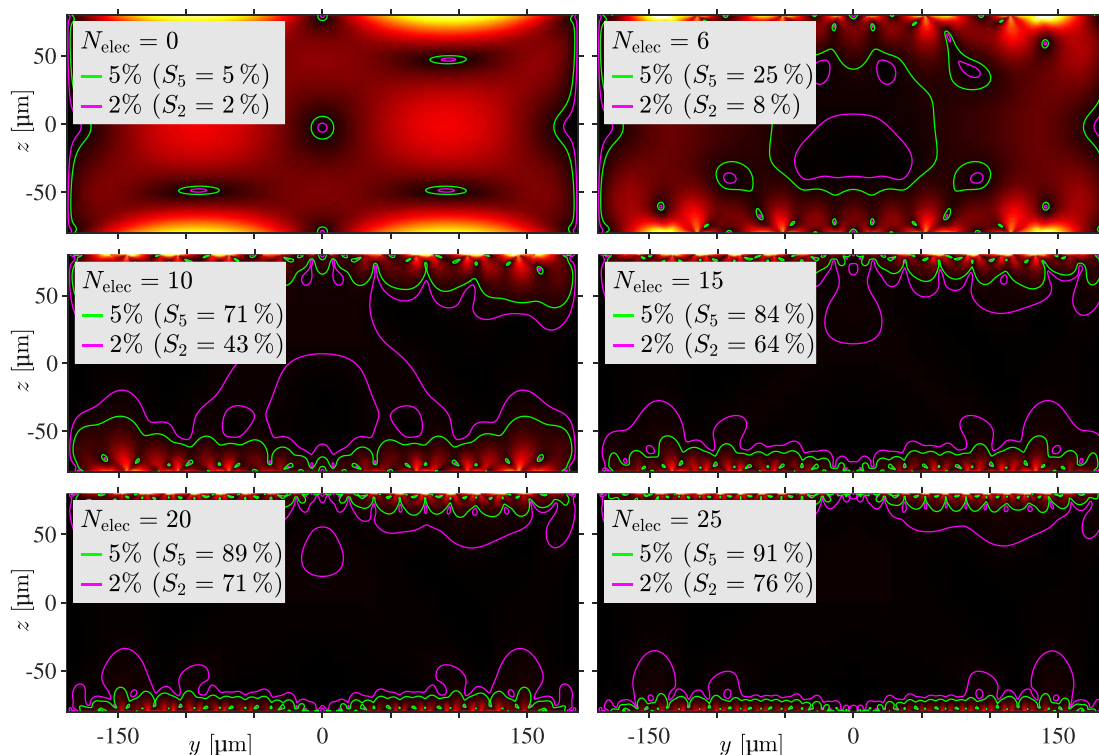


FIG. 8. (Color online) Numerical simulation of the electroacoustic streaming $\langle v_2 \rangle$, Eq. (33) and Fig. 6, as a function of electrode number N_{elec} from 0 (purely acoustic streaming) to 6, 10, 15, 20, and 25. Here, $|\langle v_2 \rangle|$, S_2 , and S_5 are plotted as in Figs. 2 and 4(c).

suggests that one can look for a reasonable trade-off between having many electrodes and reaching a high suppression.

The simulated suppressed streaming is shown in Fig. 8 for $N_{\text{elec}} = 0, 6, 10, 15, 20$, and 25. We notice that the acoustic streaming at $N_{\text{elec}} = 0$ is almost identical to the idealized mode in Fig. 2. For $N_{\text{elec}} = 10$, the entire central part of the acoustophoretic channel is cleared for streaming amplitudes above 5% of v^{Rayl} . At $N_{\text{elec}} = 15$, a similar result is seen for the 2% contour lines. Further increases in the electrode count largely just bring the contour lines closer to the boundaries. It is likely undesirable to perform particle focusing close to the boundaries regardless, as this brings adhesion effects into the problem, so increasing the number of electrodes beyond a certain point appears redundant. Right at the boundaries, high streaming velocities are still seen, but these decay on the length scale of the electrode widths. This is expected from the classical Rayleigh solutions, which find an exponential decay in boundary-driven streaming with a characteristic length scale identical to the parallel variations in the slip velocity.²⁰

VI. DISCUSSION AND CONCLUSION

We have already addressed many of the technicalities associated with the method of combining acoustic and electroosmotic streaming. Here, before concluding, we will briefly address two critical points that were neglected in the preceding analysis. First, our analysis of electroosmotic streaming was based on the assumption of a vanishing intrinsic zeta potential. However, the presence of chemically

generated charge on relevant interfaces like water/glass is inevitable. Typical values of the zeta potential for borosilicate glass are on the order of $\zeta \sim -100$ mV,⁴⁸ comparable in amplitude to the applied potentials. It is unclear whether a dc-offset of this intrinsic wall potential at the discrete electrode arrays would fully nullify its presence, as chemical charges would still form a significant charge cloud in the gaps between electrodes. One idea could be to make these gaps as small as possible.

The intrinsic zeta potential is typically modeled as a constant surface potential, and in the framework of the linearized theory, this would act as a zeroth-order field, yielding non-zero gradients in c_0 and generating a corresponding initial steady electric equilibrium potential $\phi_{0,\text{fl}}$. As noted in Ref. 49, the presence of these extra fields will lower the acquired slip velocity. A supplemental numerical study in the linearized regime by the authors suggests that the inclusion of a relatively high intrinsic zeta potential of $\zeta = -100$ mV almost halves the slip velocity of the solution used in this paper with the shape remaining the same.

Second, we only worked with 2D systems in our present study. Whereas the electroosmotic problem could in principle be implemented invariant along the channel, we know from previous experimental studies⁵⁰ that even long, straight microchannels with rectangular cross sections exhibit axial inhomogeneities in the acoustic fields, which renders a 3D analysis necessary for complete characterization of the system. Such a break in the 2D symmetry may yield areas of non-suppressed streaming, which could compromise the performance of the suggested chip design.

In conclusion, we have presented the theoretical framework for a method to effectively suppress acoustic streaming by superposing electroosmotic streaming. We have suggested a specific set of boundary conditions that achieves this suppression in a typical microchannel with a resonant standing half-wave. This idealized electroosmotic mode was then tested in an idealized hard-walled model of the microchannel; in a more realistic model including the transducer, the elastic solid, and the microchannel; and for applied voltages in both the linear and nonlinear regime.

Furthermore, we have demonstrated that the electroosmotic streaming pattern derived from a linearized theory largely holds true for relevant amplitudes of applied voltages. Last, we also evaluated numerically the capability for suppressing streaming of a specific acoustophoretic chip, where integrated discrete electrodes for generating electroosmosis were implemented. We hope that this theoretical work will inspire the acoustofluidic community to investigate experimentally the possibility of suppressing acoustic streaming in a controlled manner by electroosmosis.

¹F. Petersson, L. Åberg, A. M. Swärd-Nilsson, and T. Laurell, “Free flow acoustophoresis: Microfluidic-based mode of particle and cell separation,” *Anal. Chem.* **79**(14), 5117–5123 (2007).
²O. Manneberg, B. Vanherberghen, J. Svennebring, H. M. Hertz, B. Önfelt, and M. Wiklund, “A three-dimensional ultrasonic cage for characterization of individual cells,” *Appl. Phys. Lett.* **93**(6), 063901–063903 (2008).
³X. Ding, Z. Peng, S.-C. S. Lin, M. Geri, S. Li, P. Li, Y. Chen, M. Dao, S. Suresh, and T. J. Huang, “Cell separation using tilted-angle standing surface acoustic waves,” *Proc. Natl. Acad. Sci. U.S.A.* **111**(36), 12992–12997 (2014).
⁴B. Hammarström, T. Laurell, and J. Nilsson, “Seed particle enabled acoustic trapping of bacteria and nanoparticles in continuous flow systems,” *Lab Chip* **12**, 4296–4304 (2012).
⁵M. Evander, O. Gidlöf, B. Olde, D. Erlinge, and T. Laurell, “Non-contact acoustic capture of microparticles from small plasma volumes,” *Lab Chip* **15**, 2588–2596 (2015).
⁶D. J. Collins, C. Devendran, Z. Ma, J. W. Ng, A. Neild, and Y. Ai, “Acoustic tweezers via sub-time-of-flight regime surface acoustic waves,” *Sci. Adv.* **2**(7), e1600089 (2016).
⁷H. G. Lim, Y. Li, M.-Y. Lin, C. Yoon, C. Lee, H. Jung, R. H. Chow, and K. K. Shung, “Calibration of trapping force on cell-size objects from ultrahigh-frequency single-beam acoustic tweezer,” *IEEE Trans. Ultrason. Ferroelectr. Freq. Control* **63**(11), 1988–1995 (2016).
⁸D. Baresch, J.-L. Thomas, and R. Marchiano, “Observation of a single-beam gradient force acoustical trap for elastic particles: Acoustical tweezers,” *Phys. Rev. Lett.* **116**, 024301 (2016).
⁹P. Augustsson, C. Magnusson, M. Nordin, H. Lilja, and T. Laurell, “Microfluidic, label-free enrichment of prostate cancer cells in blood based on acoustophoresis,” *Anal. Chem.* **84**(18), 7954–7962 (2012).
¹⁰M. Antfolk, C. Magnusson, P. Augustsson, H. Lilja, and T. Laurell, “Acoustofluidic, label-free separation and simultaneous concentration of rare tumor cells from white blood cells,” *Anal. Chem.* **87**(18), 9322–9328 (2015).
¹¹M. Antfolk, P. B. Muller, P. Augustsson, H. Bruus, and T. Laurell, “Focusing of sub-micrometer particles and bacteria enabled by two-dimensional acoustophoresis,” *Lab Chip* **14**, 2791–2799 (2014).
¹²S. Li, F. Ma, H. Bachman, C. E. Cameron, X. Zeng, and T. J. Huang, “Acoustofluidic bacteria separation,” *J. Micromech. Microeng.* **27**(1), 015031 (2017).
¹³P. Augustsson, J. T. Karlsen, H.-W. Su, H. Bruus, and J. Voldman, “Iso-acoustic focusing of cells for size-insensitive acousto-mechanical phenotyping,” *Nat. Commun.* **7**, 11556 (2016).
¹⁴L. V. King, “On the acoustic radiation pressure on spheres,” *Proc. R. Soc. Lond. Ser. A* **147**(861), 212–240 (1934).

¹⁵K. Yosioka and Y. Kawasima, “Acoustic radiation pressure on a compressible sphere,” *Acustica* **5**, 167–173 (1955).
¹⁶A. A. Doinikov, “Acoustic radiation force on a spherical particle in a viscous heat-conducting fluid. I. General formula,” *J. Acoust. Soc. Am.* **101**(2), 713–721 (1997).
¹⁷M. Settnes and H. Bruus, “Forces acting on a small particle in an acoustical field in a viscous fluid,” *Phys. Rev. E* **85**, 016327 (2012).
¹⁸J. T. Karlsen and H. Bruus, “Forces acting on a small particle in an acoustical field in a thermoviscous fluid,” *Phys. Rev. E* **92**, 043010 (2015).
¹⁹P. B. Muller, M. Rossi, A. G. Marín, R. Barnkob, P. Augustsson, T. Laurell, C. J. Kähler, and H. Bruus, “Ultrasound-induced acoustophoretic motion of microparticles in three dimensions,” *Phys. Rev. E* **88**(2), 023006 (2013).
²⁰Lord Rayleigh, “On the circulation of air observed in Kundt’s tubes, and on some allied acoustical problems,” *Philos. Trans. R. Soc. Lond.* **175**, 1–21 (1884).
²¹H. Schlichting, “Berechnung ebener periodischer Grenzschichtströmungen” (“Calculation of plane periodic boundary layer streaming”), *Phys. Z.* **33**, 327–335 (1932).
²²P. Westervelt, “The theory of steady rotational flow generated by a sound field,” *J. Acoust. Soc. Am.* **25**(1), 60–67 (1953).
²³W. L. Nyborg, “Acoustic streaming near a boundary,” *J. Acoust. Soc. Am.* **30**(4), 329–339 (1958).
²⁴P. B. Muller, R. Barnkob, M. J. H. Jensen, and H. Bruus, “A numerical study of microparticle acoustophoresis driven by acoustic radiation forces and streaming-induced drag forces,” *Lab Chip* **12**, 4617–4627 (2012).
²⁵R. Barnkob, P. Augustsson, T. Laurell, and H. Bruus, “Acoustic radiation- and streaming-induced microparticle velocities determined by microparticle image velocimetry in an ultrasound symmetry plane,” *Phys. Rev. E* **86**, 056307 (2012).
²⁶C. Lee and T. Wang, “Near-boundary streaming around a small sphere due to 2 orthogonal standing waves,” *J. Acoust. Soc. Am.* **85**(3), 1081–1088 (1989).
²⁷J. Vanneste and O. Bühler, “Streaming by leaky surface acoustic waves,” *Proc. R. Soc. A* **467**(2130), 1779–1800 (2011).
²⁸J. S. Bach and H. Bruus, “Theory of pressure acoustics with viscous boundary layers and streaming in curved elastic cavities,” *J. Acoust. Soc. Am.* **144**, 766–784 (2018).
²⁹C. Eckart, “Vortices and streams caused by sound waves,” *Phys. Rev.* **73**, 68–76 (1948).
³⁰J. S. Bach and H. Bruus, “Bulk-driven acoustic streaming at resonance in closed microcavities,” *Phys. Rev. E* **100**, 023104 (2019).
³¹T. M. Squires and M. Z. Bazant, “Induced-charge electro-osmosis,” *J. Fluid Mech.* **509**(1), 217–252 (2004).
³²A. Ajdari, “Pumping liquids using asymmetric electrode arrays,” *Phys. Rev. E* **61**(1), R45–R48 (2000).
³³A. B. D. Brown, C. G. Smith, and A. R. Rennie, “Pumping of water with ac electric fields applied to asymmetric pairs of microelectrodes,” *Phys. Rev. E* **63**(1), 016305 (2000).
³⁴M. M. Gregersen, L. H. Olesen, A. Brask, M. F. Hansen, and H. Bruus, “Flow reversal at low voltage and low frequency in a microfabricated ac electrokinetic pump,” *Phys. Rev. E* **76**(5), 056305 (2007).
³⁵M. Wiklund, P. Spégel, S. Nilsson, and H. M. Hertz, “Ultrasonic-trap-enhanced selectivity in capillary electrophoresis,” *Ultrasonics* **41**(4), 329–333 (2003).
³⁶N. R. Skov, J. S. Bach, B. G. Winkelmann, and H. Bruus, “3D modeling of acoustofluidics in a liquid-filled cavity including streaming, viscous boundary layers, surrounding solids, and a piezoelectric transducer,” *AIMS Math.* **4**, 99–111 (2019).
³⁷P. B. Muller and H. Bruus, “Numerical study of thermoviscous effects in ultrasound-induced acoustic streaming in microchannels,” *Phys. Rev. E* **90**(4), 043016 (2014).
³⁸P. B. Muller and H. Bruus, “Theoretical study of time-dependent, ultrasound-induced acoustic streaming in microchannels,” *Phys. Rev. E* **92**, 063018 (2015).
³⁹R. Zana and E. B. Yeager, “Ultrasonic vibration potentials,” in *Modern Aspects of Electrochemistry*, edited by J. O. Bockris, B. E. Conway, and R. E. White (Springer US, Boston, MA, 1982), pp. 1–60.
⁴⁰J. Voldman, “Electrical forces for microscale cell manipulation,” *Annu. Rev. Biomed. Eng.* **8**(1), 425–454 (2006).
⁴¹See supplementary material at <https://www.scitation.org/doi/suppl/10.1121/10.0005051> for details on the values of the material parameters and on the COMSOL mesh convergence study.

- ⁴²J. S. Bach and H. Bruus, "Suppression of acoustic streaming in shape-optimized channels," *Phys. Rev. Lett.* **124**, 214501 (2020).
- ⁴³N. Mortensen, L. Olesen, L. Belmon, and H. Bruus, "Electrohydrodynamics of binary electrolytes driven by modulated surface potentials," *Phys. Rev. E* **71**, 056306 (2005).
- ⁴⁴M. S. Kilic, M. Z. Bazant, and A. Ajdari, "Steric effects in the dynamics of electrolytes at large applied voltages. II. Modified Poisson-Nernst-Planck equations," *Phys. Rev. E* **75**, 021503 (2007).
- ⁴⁵W. H. Press, S. A. Teukolsky, W. T. Vetterling, and B. P. Flannery, *Numerical Recipes in C: The Art of Scientific Computing*, 2nd ed. (Cambridge University, Cambridge, UK, 2002).
- ⁴⁶COMSOL Multiphysics 5.4 (2018), <http://www.comsol.com> (Last viewed 23 April 2021).
- ⁴⁷W. N. Bodé, L. Jiang, T. Laurell, and H. Bruus, "Microparticle acoustophoresis in aluminum-based acoustofluidic devices with PDMS covers," *Micromachines* **11**(3), 292 (2020).
- ⁴⁸B. J. Kirby and E. F. Hasselbrink, Jr., "Zeta potential of microfluidic substrates: 2. Data for polymers," *Electrophoresis* **25**(2), 203–213 (2004).
- ⁴⁹L. H. Olesen, H. Bruus, and A. Ajdari, "ac electrokinetic micropumps: The effect of geometrical confinement, faradaic current injection, and nonlinear surface capacitance," *Phys. Rev. E* **73**(5), 056313 (2006).
- ⁵⁰P. Augustsson, R. Barnkob, S. T. Wereley, H. Bruus, and T. Laurell, "Automated and temperature-controlled micro-PIV measurements enabling long-term-stable microchannel acoustophoresis characterization," *Lab Chip* **11**(24), 4152–4164 (2011).